Ultraviolet Laser Absorption Imaging of High-Speed Flows in a Shock Tube

Lingzhi Zheng*[†], Adam J. Susa[†], Ajay Krish[†], and Ronald K. Hanson [‡] Stanford university, Stanford, California, 94305, USA

Observation of high-speed reactive flows using laser-absorption-based imaging techniques is of interest for its potential to quantitatively reveal both gas-dynamic and thermochemical processes. In the current study, an ultraviolet (UV) laser-absorption imaging method based on nitric oxide (NO) is demonstrated to capture transient flows in a shock tube. A tunable laser was used to generate a continuous-wave UV beam at 226.1019 nm to coincide with a strong NO absorption feature. The UV beam was expanded to a 20-mm diameter and routed through the shock tube to image the flow adjacent to the end wall. Time-resolved imaging was realized using a Lambert HiCATT high-speed UV intensifier coupled to a Phantom v2012 high-speed camera. Static absorbance measurements of 1.97% NO/Ar mixtures were first performed to validate the proposed imaging concept, showing good agreement with values predicted by a spectroscopic model. UV laser-absorption images of incident and reflected shock waves captured at 90 kHz temporal resolution are then reported. Translational temperature profiles across the incident and reflected shocks calculated from absorbance images show reasonable agreement with calculated values. After the passage of the reflected shock wave, the flow near the end wall was monitored to probe the development of the end-wall thermal boundary layer. Thermometry measurements across the thermal boundary layer show good agreement with analytical solutions. This study demonstrates the potential of UV laser-absorption imaging in high-speed flow fields, to be applied to more complex applications in the future.

I. Nomenclature

 α = absorbance

 σ_{NO} = NO absorption cross-section T_{tr} = translational temperature T_{vib} = vibrational temperature

P = pressure

 λ = laser wavelength

n = number density of the gas mixture

 X_{NO} = mole fraction of NO

L = path length

 $I_{\rm o}$ = full measurement intensity

 $I_{\rm a}$ = absorption measurement intensity

 $I_{\rm d}$ = dark measurement intensity

 T_1 = region-1 temperature (initial fill condition) T_2 = region-2 temperature (post incident shock) T_5 = region-5 temperature (post reflected shock) P_1 = region-1 pressure (initial fill condition) P_2 = region-2 pressure (post incident shock)

P₅ = region-5 pressure (post reflected shock)
S = translational temperature sensitivity

f = generic function

^{*}Corresponding Author: liz147@stanford.edu

[†]Graduate Research Assistant, Department of Mechanical Engineering

[‡]Professor, Department of Mechanical Engineering, Fellow AIAA

II. Introduction

In the extreme conditions encountered in high-speed reactive flows, thermochemical processes, such as vibrational nonequilibrium and chemical reactions, and gas-dynamic processes, such as shock wave dynamics and boundary layer effects, are coupled and of joint interest. Hence, an optimal diagnostic should provide spatially and temporally resolved insights into both gas-dynamic and thermochemical processes. Many imaging approaches have been developed for such purposes. Schlieren imaging is a popular line-of-sight (LOS) technique based on the deflection of light through index of refraction gradients in the flow field [1] [2]. Due to its high spatial and temporal resolutions, schlieren imaging has been utilized in numerous studies to obtain positional measurements of flow features [3]-[7]. However, extracting quantitative density distributions remains challenging due to difficulties in the precise calibration of grayscale schlieren images [8]. While specialized rainbow schlieren techniques are capable of providing density and temperature profiles in some flow fields [8]-[10], meticulous calibrations of schlieren stops are still required. Planar laser-induced fluorescence (PLIF) imaging is a laser-based alternative to LOS beam-steering-based methods such as schlieren. Unlike schlieren imaging, which can only measure properties that are related to the index of refraction, PLIF can reveal spatially resolved species concentrations as well as thermodynamic conditions of the flow [5] [6] [1]-[13]. However, in-situ calibration is generally needed for quantitative data interpretations, once again making quantitative measurements difficult to obtain [13]. In this context, an alternative technique that is quantitative and does not require rigorous calibrations becomes desirable.

As a quantitative, calibration-free technique well established for making LOS measurements of highly dynamic thermochemical processes [14], laser absorption spectroscopy (LAS) is an attractive alternative to schlieren and PLIF. While most applications of LAS are single-path measurements, numerous past studies have investigated extending LAS to 2-dimensional (2D) laser absorption imaging (LAI) [15]-24]. Liu et. al and Wei et. al obtained topographically reconstructed flow images by using a single line-of-sight mid-infrared (mid-IR) laser with the flow field on translating mechanical stages [15] [16]. Ma et. al and Foo et. al adopted a similar tomographic approach but utilized split laser beams and detector arrays to achieve higher temporal resolutions [17] [19]. While mid-IR tomographic imaging obtained from laser absorption measurements offers potential for full-field property information, its temporal resolution is generally limited [23], and complex data processing is required for reconstructing the final image. Motivated by the shortcomings of these multi-point strategies, laser absorption imaging using expanded laser beams and high-speed IR cameras was developed [22]-24]. The addition of high-speed IR cameras significantly increased the spatial and temporal resolution of mid-IR LAI, enabling an image acquisition rate up to 2 kHz [23]. However, despite the improvements, LAI in mid-IR has currently only been applied to steady-state or relatively low-speed flows such as burner flames, and the kHz temporal resolution remains insufficient for imaging more dynamic environments such as supersonic and hypersonic flows.

In addition to LAI performed in the mid-IR, absorption imaging has also been explored in the ultraviolet (UV). Utilizing broadband flashlamps and lasers with UV-intensified cameras, Qi et. al and Zhang et. al obtained full-field vapor concentrations and temperature profiles in fuel sprays [25]—30]. Unlike the IR cameras used in current LAI literature, which have usable temporal resolutions limited to the kHz range [23], UV intensifiers are capable of producing temporal resolutions in the order of 10 kHz - 1 MHz [28] [31]—33]. However, this advantage of UV intensifiers has not yet been fully exploited in the studies of fuel sprays as the reported results are primarily single-shot images. The application of UV absorption imaging to flow fields beyond fuel sprays, and utilizing narrow-linewidth laser sources to provide quantum-state, species-specific imaging also merits further investigation.

The current work proposes a quantitative, calibration-free UV laser-absorption imaging (UV-LAI) technique with sufficient capability to spatially and temporally resolve properties of highly dynamic, uniform LOS flow fields. UV absorption of nitric oxide (NO) at 226.1019 nm was selected as the basis for the proposed imaging concept. As NO is an important species that naturally forms at the high temperature encountered in combustion processes and hypersonic flows [34-37], using NO as the target species opens up potential diagnostic opportunities for broader real-world applications where flow seeding is not feasible. NO also has relatively high absorbance in the UV spectrum with relatively low interference from other species at temperatures below 2,000 K [34, 38] making it attractive for quantitative measurements.

III. Method

A. Static and Shock Tube Experiments

Both static and shock tube experiments were performed in a circular cross-section, optically accessible shock tube described in detail by Campbell et al [39]. The shock tube has a variable driver section designed to achieve different

experimental test times. The driven section of the shock tube, consisting of a buffer section and a constrained-reaction-volume (CRV) section, has an inner diameter of 11.53 cm and is 9.76-m long. The CRV section was recently redesigned with UV-grade optical windows to allow imaging of flows up to the shock tube end wall.

Static experiments were conducted by filling the isolated CRV section with a mixture of argon seeded with 1.97% NO at room temperature and different fill pressures, listed in Table 1.

Table 1 Fill pressures of 1.97% NO, balance of argon mixture used in static experiments.

Experimental Trial	1	2	3
Fill Pressure	2.11 torr	5.04 torr	12.18 torr

A reflected-shock experiment was performed with 0.2% seeding of NO in argon. The incident shock speed was measured from pressure transducer responses and used to calculate the initial bulk-gas thermodynamic conditions behind the incident and reflected shocks using the FROSH code described in [40]. The following assumptions were made on the vibrational state of the test gas during condition calculations. Within region 1, the test gas was assumed to be at vibrational equilibrium ($T_{tr,1} = T_{vib,1} = T_1$). In the post-incident-shock region 2, the test gas was assumed to be vibrationally frozen, with the NO vibrational temperature remaining at $T_{vib,1}$. This assumption was adopted because the maximum region-2 particle time within the laser LOS (\sim 140 μ s) was sufficiently small compared to the literature-extracted characteristic vibrational relaxation time of this NO mixture (\sim 560 μ s) [41]. Additionally, as the mixture was highly dilute in argon, any NO vibrational relaxation in region 2 would not significantly impact the initial bulk-gas translational temperatures. The FROSH-calculated initial translational temperature and pressure at regions 2 and 5, as well as the initial conditions of region 1, are listed in Table [2]. The shock conditions were selected such that the test gas would remain chemically frozen throughout the experiment.

Table 2 Initial thermodynamic conditions during the reflected-shock experiment.

Region	1	2	5
Translational Temperature	296 K	581 K	938 K
Pressure	0.035 atm	0.15 atm	0.46 atm

B. UV Laser Absorption Spectroscopy

The foundational principle underlying path-integrated absorption spectroscopy of monochromatic light, the Beer-Lambert Law, is expressed for the interference-free absorption of NO in Eq. (I):

$$\alpha = \sigma_{\text{NO}}(T_{\text{tr}}, T_{\text{vib}}, P, \lambda) n X_{\text{NO}} L \tag{1}$$

where α is the absorbance, σ_{NO} is the NO absorption cross-section, n is the total number density of the gas mixture, X_{NO} is the NO mole fraction, and L is the path length. The NO absorption cross-section, σ_{NO} , is dependent on the NO translational temperature, T_{tr} , the NO vibrational temperature, T_{vib} , pressure, P, and laser wavelength λ . At a given condition, the NO absorption cross-section was obtained from a spectroscopic model constructed for the NO (0,0) γ -band, details of which are provided in [42].

Absorbance is calculated pixel-wise from image intensities through Eq. (2):

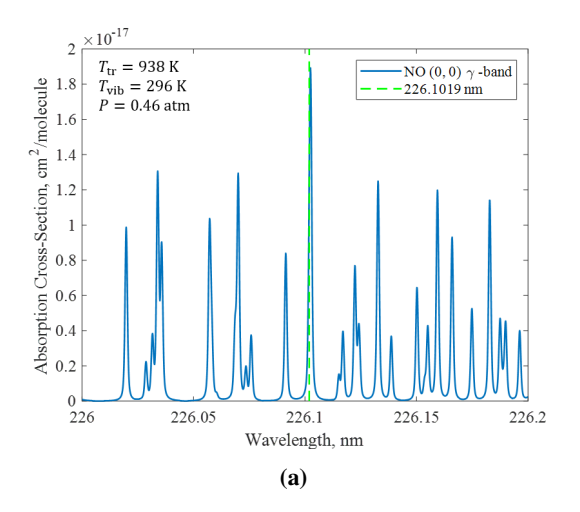
$$\alpha = -\ln\left(\frac{I_{\rm a} - I_{\rm d}}{I_{\rm o} - I_{\rm d}}\right) \tag{2}$$

where I_a is the transmitted laser intensity after absorption, I_o is the laser intensity without absorption and I_d is the background intensity without the laser.

From Eq. (I), n, X_{NO} , L, P, and λ are known, leaving α related to only T_{tr} and T_{vib} . Therefore, if T_{vib} can be assumed or related to T_{tr} through an energy argument, the single-wavelength absorbance can be used as the basis of thermometry measurements, as reported in this work. In future reactive applications in which X_{NO} and/or T_{vib} might be unknown, two laser wavelengths could be adopted to simultaneously measure temperature and concentration, or both T_{tr} and T_{vib} .

C. Wavelength Selection

A laser wavelength of 226.1019 nm, comprised of the (0,0) Q11(12.5), R12(19.5), P21(12.5), Q22(19.5) lines, was adopted for the current study from selections made for high-temperature experiments in [42]. The modeled NO absorption cross-sections at the initial and vibrationally equilibrated region-5 conditions are shown in Fig. [1].



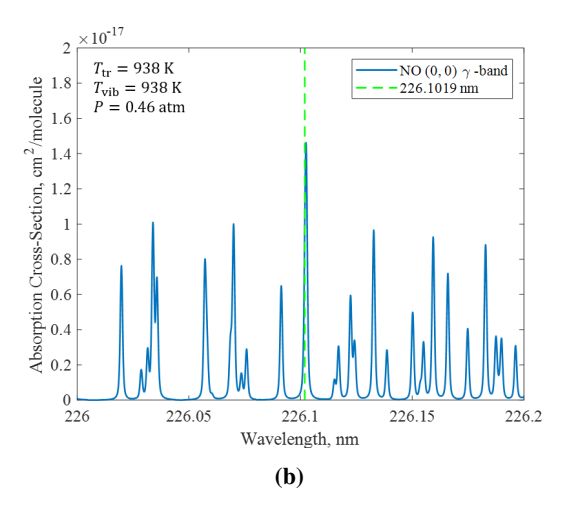
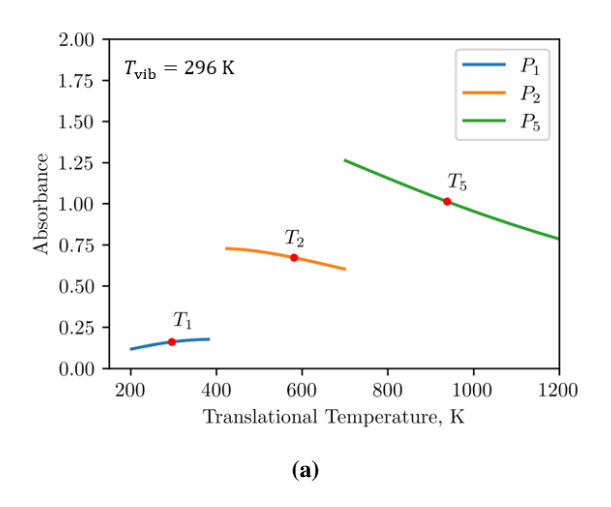


Fig. 1 Modeled NO absorption cross-sections at the a) initial and b) vibrationally equilibrated region-5 conditions.

Figure 2 a) shows the absorbance response as functions of translational temperature calculated using modeled NO absorption cross-sections at conditions near regions 1, 2, and 5. As the adopted wavelength was originally chosen for a diagnostic developed for temperatures ranging from 2,000 K to 6,000 K, it was not optimized for the 300 K to 1,000 K conditions of the current experiments. However, the wavelength still gives reasonable absorbance levels of 0.7 and 1.1 at region-2 and -5 conditions and was the most practically accessible laser wavelength at the time of experiments. To assess the measurement sensitivity of the selected wavelength, the translational temperature sensitivity of absorbance, *S*, was calculated with Eq. (3):

$$S = \left| \frac{d\alpha}{\alpha} \frac{T_{\rm tr}}{dT_{\rm tr}} \right| \tag{3}$$



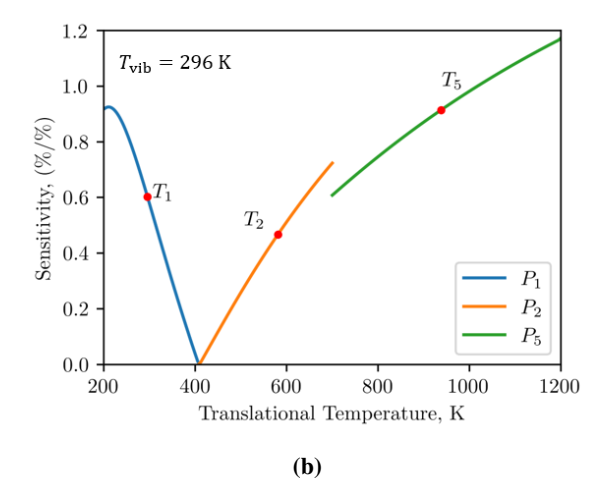


Fig. 2 a) Calculated absorbance as a function of translational temperature. b) Temperature sensitivities of absorbance at the 226.1019 nm diagnostic wavelength. The expected absorbances and sensitivities at regions 1, 2, and 5 are shown in red markers.

where S indicates the percent change in absorbance for a unit percent change in translational temperature. The translational temperature sensitivities at regions 1, 2, and 5 are shown in Fig. $\boxed{2}$ b).

Figure 2 b) reveals that the region-5 condition had the highest sensitivity with a unit percent change in translational temperature leading to a 0.9% percent change in absorbance, but the sensitivities at regions 1 were relatively low (0.6 and 0.5 respectively). While the sensitivity yielded by the current wavelength was not optimal, it could still produce resolvable absorbance features in the static and shock tube experiments, and hence, was sufficient for proof-of-concept demonstrations. In future studies, the translational temperature sensitivity is expected to improve with a more optimally selected laser wavelength.

In addition to the translational temperature sensitivity, the translational temperature uncertainties for given absorbance uncertainties could be estimated using the NO spectroscopic model through Eq. (4):

$$\frac{\Delta T_{\rm tr}}{T_{\rm tr}} = \frac{\Delta \alpha}{\alpha} \left| \frac{dT_{\rm tr}}{T_{\rm tr}} \frac{\alpha}{d\alpha} \right| = \frac{\Delta \alpha}{\alpha} \frac{1}{S}$$
 (4)

where $\Delta T_{\rm tr}/T_{\rm tr}$ and $\Delta \alpha/\alpha$ are the fractional uncertainties in translational temperature and absorbance. With a representative 1- σ absorbance uncertainty of 0.03, the uncertainties in translational temperatures in regions 1, 2, and 5 were calculated as 57 K, 49 K, and 31 K using Eq. 4 Lower absorbance uncertainties will yield proportionally smaller uncertainties in $T_{\rm tr}$.

D. UV Laser Absorption Imaging System

The schematic of the UV-LAI setup is shown in Fig. [3]. The UV beam was produced by an M-Squared laser system utilizing two cascaded frequency doubling stages to convert the input near-infrared (NIR) light to a tunable UV beam. A 532-nm Nd:YAG laser (Coherent Verdi V18) pumped a Ti:Sapphire module (M-Squared SolsTiS) to generate the tunable NIR which was then routed into the cascaded frequency doubling stages (M-Squared ECD-X and ECD-X-Q) to yield coherent and continuous-wave UV light.

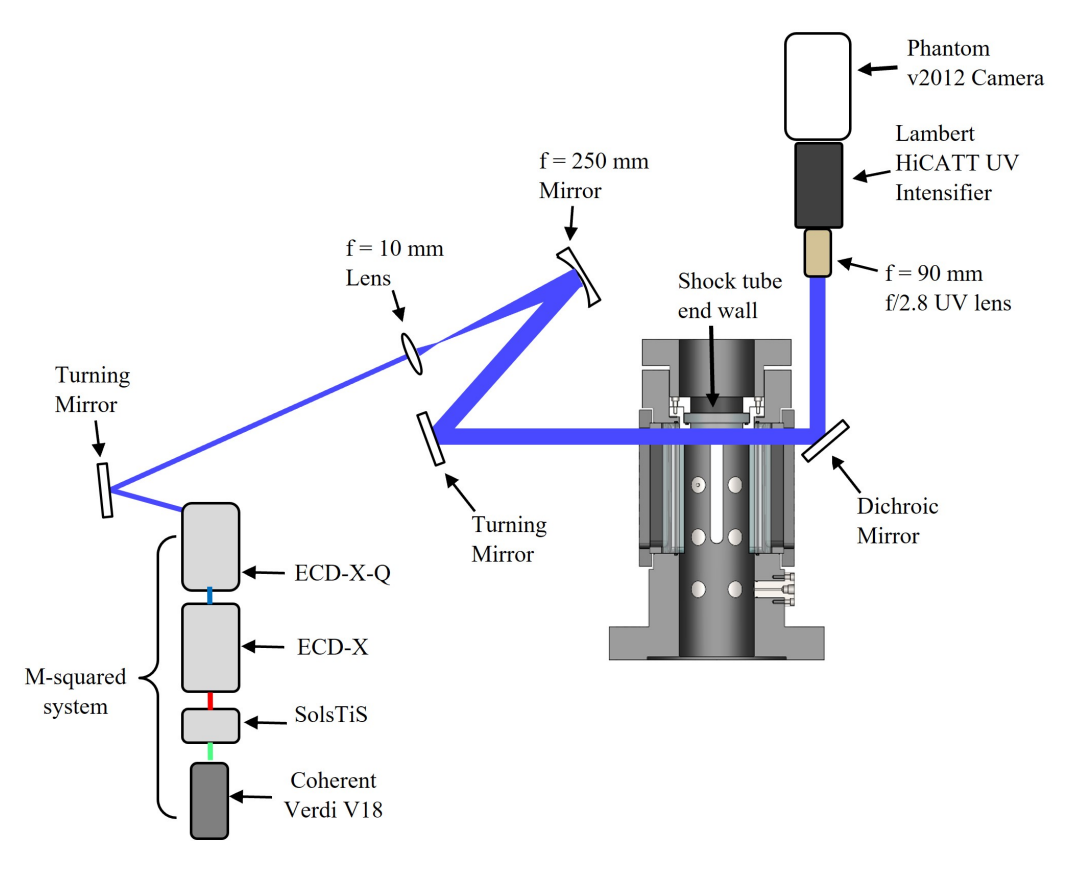


Fig. 3 Schematic of the optical configuration used for UV-LAI.

The UV beam diameter produced by the M-squared system was 0.8 mm, which was then expanded by a 10 mm focal length lens and a 250 mm focal length mirror to a diameter of 20 mm. The expanded beam was turned and aligned through a pair of side-wall optical windows on the shock tube, resulting in a final field-of-view (FOV) with an elliptical shape. The distance between the shock tube end wall and the edge of the FOV, inferred from the propagation of the incident and reflected shock waves, was 0.26 mm. After the UV beam exited the shock tube, a dichroic mirror was used to reject potential visible interference. High-speed imaging of the transmitted UV beam was enabled by a UV intensifier (Lambert HiCATT) coupled to a high-speed CMOS camera (Phantom v2012). The laser irradiance received by the UV intensifier without absorption was 0.30 mW/cm². The camera frame rate and the UV intensifier gating time were set to 100 Hz and 350 ns for the static experiments and 90 kHz and 1 µs for the reflected-shock experiment. To avoid beam steering caused by flow-induced density gradients, the imaging system was focused to the center of the shock tube as recommended by Greenberg and Westlye et. al [43, 44]. A 128- by 128-pixel sensor region was recorded at 47 pixel/cm resolution.

Three image sequences were recorded as a part of each experiment. First, a full measurement, I_0 , was made with the shock tube maintained at vacuum. Then, a dark measurement, I_d , was recorded with the laser briefly blocked. Lastly, the absorption measurement of the flow, I_a , was captured during experiments.

E. Image Processing and Data Interpretation

Figure 4 illustrates the image processing routine used to extract absorbance and translational temperature images from experimental data.

Absorbance images were first calculated from the full, dark, and absorption images using Eq. (2). Spatial median filtering was then applied to the absorbance images over a 10-pixel-diameter area. In images with shock waves, the

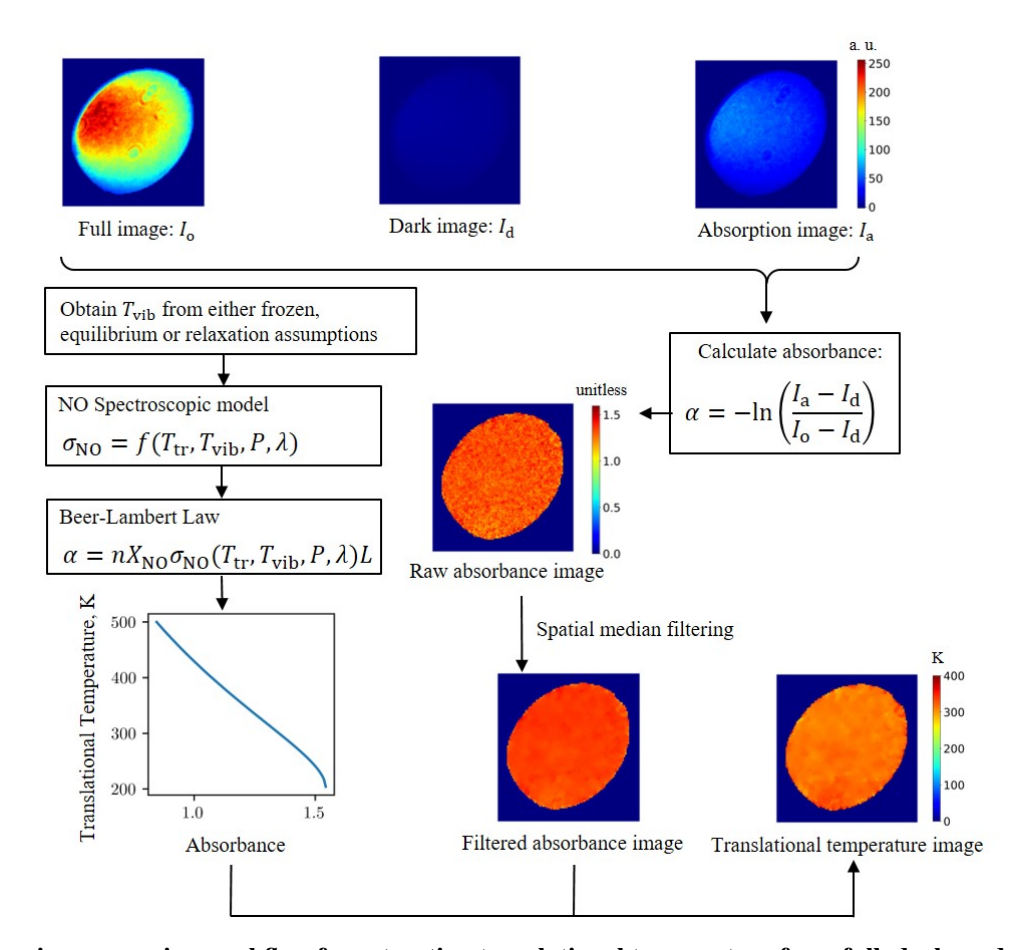


Fig. 4 Imaging processing workflow for extracting translational temperature from full, dark, and absorption images. The colors in I_0 , I_d , and I_a images represent grayscale intensity.

image regions behind and in front of the shock front were separated using the Ostu thresholding method [45] and filtered individually to avoid artificially blurring the shock fronts. With appropriate assumptions on the NO vibrational state, an interpolation function between the NO translational temperature and absorbance was constructed from the NO spectroscopic model using a presumed or calculated NO vibrational temperature. The final translational temperature images were obtained by applying the interpolation function on each pixel measurement of absorbance.

The following assumptions were applied to the NO vibrational state to obtain $T_{\rm vib}$. Behind the incident shock, NO in the mixture was assumed to be vibrationally frozen ($T_{\rm vib} = T_1$). After the passage of the reflected shock, NO was assumed to undergo vibrational relaxation with $T_{\rm vib}$ starting at T_1 . An energy argument as described by Bethe and Teller was used to calculate $T_{\rm vib}$ during vibrational relaxation. In regions with varying translational temperatures due to thermal diffusion, such as the region within the end-wall thermal boundary layer, $T_{\rm tr}$ and $T_{\rm vib}$ become functions in position as well as time. In such cases, a vibrational equilibrium assumption was applied to regions affected by thermal diffusion to obtain approximate translational temperature profiles.

It is also worth noting that Fig. 4 shows airy-disk-like interference patterns, similar to ones reported by Schwarm et. al and Tancin et. al [23] [24], in both the full and the absorption images. While special treatments were required in the cases of Schwarm et. al and Tancin et. al, the interference patterns in this study were observed to stay constant relative to their surroundings throughout the experiments, and hence, were eliminated through the application of Eq. (2) without requiring additional considerations.

IV. Results

A. Static Experiments

During each experiment, 100 consecutive intensity images were recorded. Figure 5 shows the time-averaged images of full intensity and absorption measurements (of transmitted intensity) obtained from static experiments. To assess the signal quality of the intensity images, signal-to-noise ratio (SNR), defined by the ratio between the average intensity and the standard deviation of intensities across 100 images, are characterized pixel-wise for the full and absorption images, and the results are shown in Fig. 6 Figures 6 a) and b) illustrate that a nominal SNR between 27 and 12 was achieved for an absorbance between 0 and 1.8.

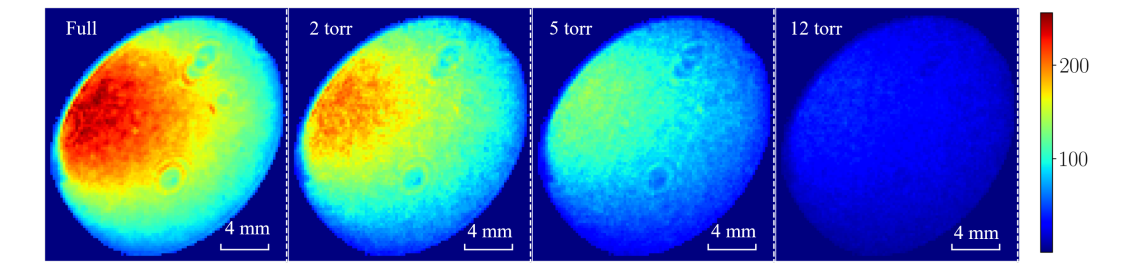


Fig. 5 Time-averaged intensity images of full (no absorption) intensity and transmitted intensity (with absorption) measurements for static experiments. The colors in the images indicate the grayscale intensity of image pixels. The white dash lines in the images represent the location of the shock tube end wall.

Temporally and spatially averaged absorbance results from each static experiment are compared with model predictions and are shown in Fig. [7]. From Fig. [7], the absorbances from the 2-torr and 5-torr experiments show good agreement with the NO spectroscopic model as the model predicted absorbances fall within the $1-\sigma$ uncertainty of the average measured absorbance. The nominal absorbance from the 12 torr measurement is observed to deviate more from the model predicted value, but this is expected to be due to the lower SNR of the 12 torr measurement.

The results from static experiments indicate the proposed UV absorption imaging diagnostic recovers expected NO absorbance values with acceptable accuracy. Additionally, both the SNR and the measurement accuracy provide clear opportunities for improvement in future studies through the better selection of laser wavelengths to maximize *S* at conditions of interest.

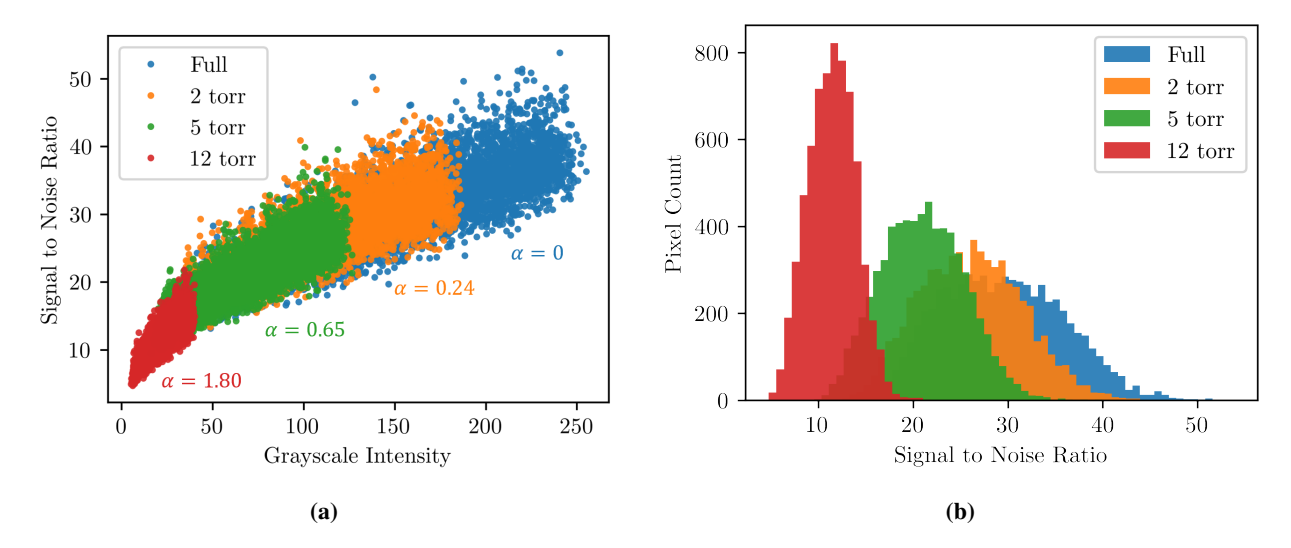


Fig. 6 a) Signal-to-noise ratio of full intensity and transmitted intensity with variable absorption measurements calculated pixel-wise as a function of the grayscale intensities of the image pixels. The mean absorbances of the data sets are also shown in a) for reference. b) Pixel count of signal-to-noise ratios in the intensity images.

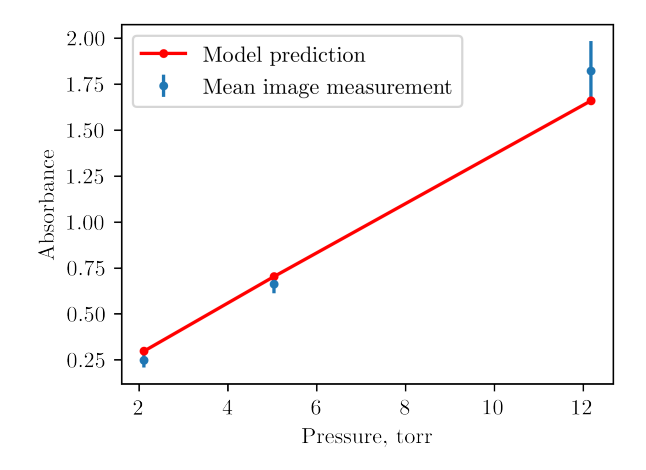


Fig. 7 Spatially and temporally averaged absorbance results from static experiments (in blue) overlaid with predicted absorbances from the NO spectroscopic model (in red).

B. Incident and Reflected Shocks

Translational temperature images of the incident and reflected shock waves obtained from the reflected-shock experiment are shown in Fig. (a) and b). The arrival of the incident shock wave at the end wall was set as time zero. The central axial translational temperature profiles across the incident and reflected shocks are shown in Fig. (a). From Fig. (a) uniform temperature fields are observed in the post-shock gas away from the shock fronts, as expected from normal shock propagation. Figure (b) illustrates that the measured translational temperatures across the reflected shock generally agree well with FROSH-calculated values, though, discrepancies in the measured and calculated translational temperatures are observed in some image regions. Behind the shock fronts, the inferred translational temperatures in the regions very close to the shock fronts are higher than those in the regions that are further away. Additionally, in the first two frames with the incident shock ($t = -24\mu s$ and $t = -13 \mu s$), the translational temperatures behind the shock are observed to be more than 100 K higher than the expected region-2 temperature.

Both of these discrepancies can be attributed to the prototype imaging setup. The first disagreement is caused by the finite contrast resolution of the optical system. While shock fronts ideally correspond to step changes in image intensity, a system with a finite contrast resolution instead produces more gradual intensity changes, leading to lower

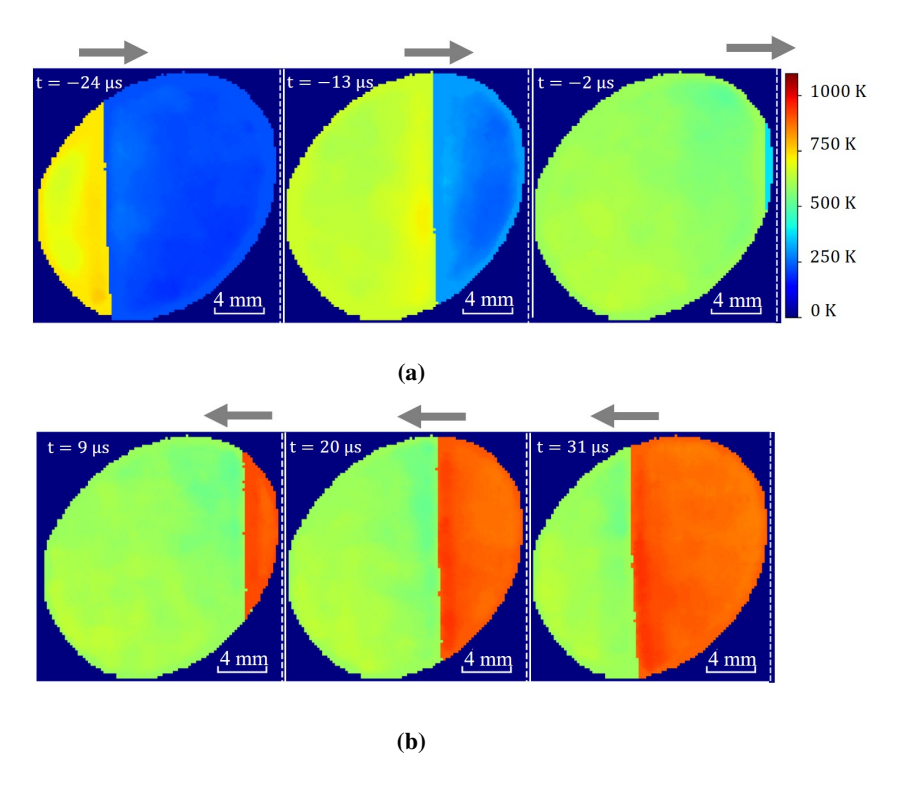


Fig. 8 Time-resolved translational temperature images of a) incident and b) reflected shock waves near the shock tube end wall (end-wall location indicated with white dash lines). The gating width of the images is 1μ s. The arrows above the images indicate the direction of shock propagation.

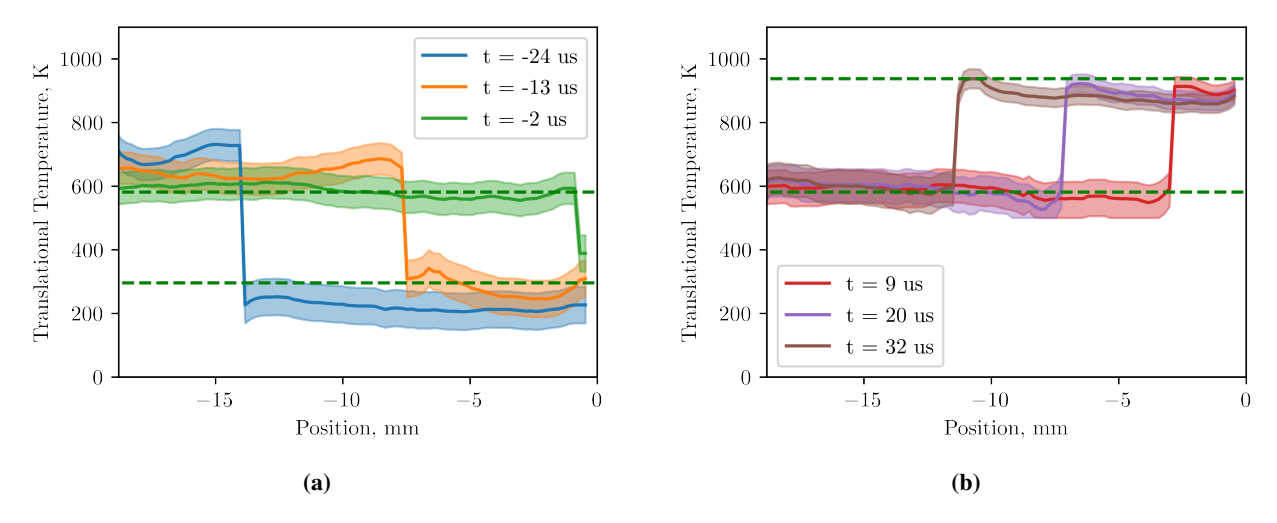


Fig. 9 Time-resolved axial translational temperature profiles across the a) incident and b) reflected shock waves. Estimated 1- σ uncertainties in translational temperature are indicated by the shaded areas in the plots. The green dash lines in a) and b) are the expected temperatures from FROSH at regions 1, 2, and 5 as listed in Table 2.

than expected absorbances immediately behind the shock fronts. Since translational temperature is inversely related to absorbance at regions 2 and 5, as indicated in Fig. 2a), these lower absorbances manifest as artificially high translational temperatures when the images were processed. The second discrepancy can possibly be attributed to a non-linear response of the UV intensifier. As UV-intensifiers are known to have non-linear responses at high incident intensities 47, 48, transient non-linearity in the UV intensifier could have resulted in the temporarily elevated temperatures in Fig.

Description This is also consistent with the time evolution with the translational temperature behind the incident shock. As the incident shock travels further into the frame, the temperature discrepancy decreases, and at $t \ge -2$ µs, the measured region-2 temperature profiles match the expected region 2 temperature.

Although the translational temperature images of the incident and reflected shock currently carry elevated uncertainties, future measurements are expected to show improvement. With an optimally selected laser wavelength, the NO translational temperature will be less sensitive to errors in absorbance, mitigating the nonphysical temperature rise caused by the finite image resolution. Characterizations of the UV intensifier's transient response will also be conducted to confirm the impact of any transient non-linearity and correct for any non-linear responses as proposed in [47].

C. End-Wall Thermal Boundary Layer

Figure $\boxed{10}$ shows the translational temperature images from t = 0.05 ms (the frame immediately after the reflected shock wave exited the FOV) to t = 4.05 ms. To demonstrate the accuracy of temperature measurements in the end-wall boundary layer, axial translational temperature profiles were extracted and compared with an analytical solution of shock tube end-wall thermal diffusion by Van Dongen $\boxed{49}$ in Fig. $\boxed{11}$

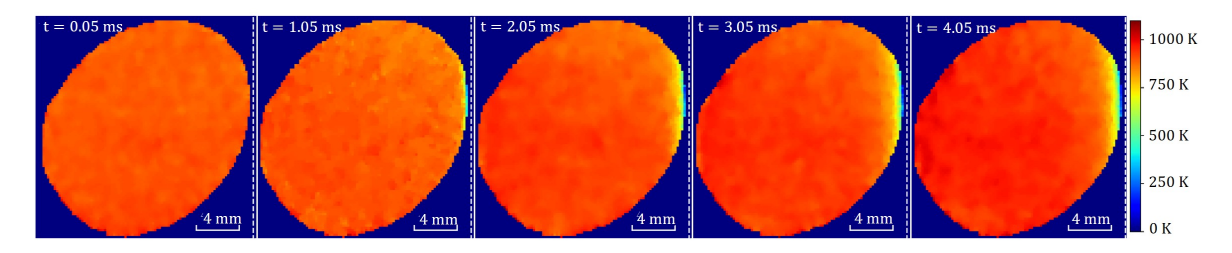


Fig. 10 Translational temperature images showing the growth of end-wall thermal boundary layer between t = 0.05 ms and t = 4.05 ms. The gating width of the images is 1 μ s. The location of the end wall is shown as a white dash line.

A uniform translational temperature field at t = 0.05 ms is observed in Fig. [10] and as time progressed, the temperature near the end wall decreased, owing to the growth of the thermal boundary layer. The temperature images show that the end-wall thermal boundary layer is thinner than 5 mm at t = 4.05 ms, implying the thermal boundary layer is unlikely to impact measurements of the bulk gas more than 5 mm away from the end wall within that time. From Fig. [11] good agreement in temperature profiles is observed between the analytical solution and image measurements for $t \ge 2.05$ ms. The temperature profiles were extracted assuming $T_{tr} = T_{vib}$ in the thermal boundary layer, as discussed in III.E; the agreement with the analytical model suggests the assumption was reasonable at longer times. In future developments of UV laser absorption imaging, multiple laser wavelengths can be utilized to extract both the NO vibrational and translational temperatures to more accurately measure temperature in the end-wall thermal boundary layer.

Unlike images of the incident and reflected shocks, the end-wall thermal boundary layer images were free of sharp intensity gradients and rapid transient changes. Therefore, the agreement between image measurements and the analytical model suggests the current proof-of-concept UV-LAI system was capable of quantitative measurements of transient phenomena with sub-millisecond time scales. However, this does not imply that the temporal resolution for the proposed imaging concept to make quantitative measurements is limited to kHz levels. As elaborated in IV.B, future improvements in wavelength selection and characterizations of the UV intensifier's transient non-linearity will greatly enhance the measurement quality at higher frame rates, pushing further the temporal resolution of highly quantitative data.

V. Conclusion

In the present work, a proof-of-concept UV-LAI diagnostic using a UV laser operating at continuous-wave with a fixed wavelength was applied to shock tube flows. Absorption imaging of NO achieved a temporal resolution of 90 kHz, improving significantly from previous LAI works performed in the mid-IR. Static validation experiments showed that the current UV-LAI implementation produced reasonably accurate full-field NO absorbances. The reflected-shock experiment presents the first time-resolved images of incident and reflected shocks captured with UV-LAI. Image-extracted axial translational temperature profiles across the incident and reflected shocks showed

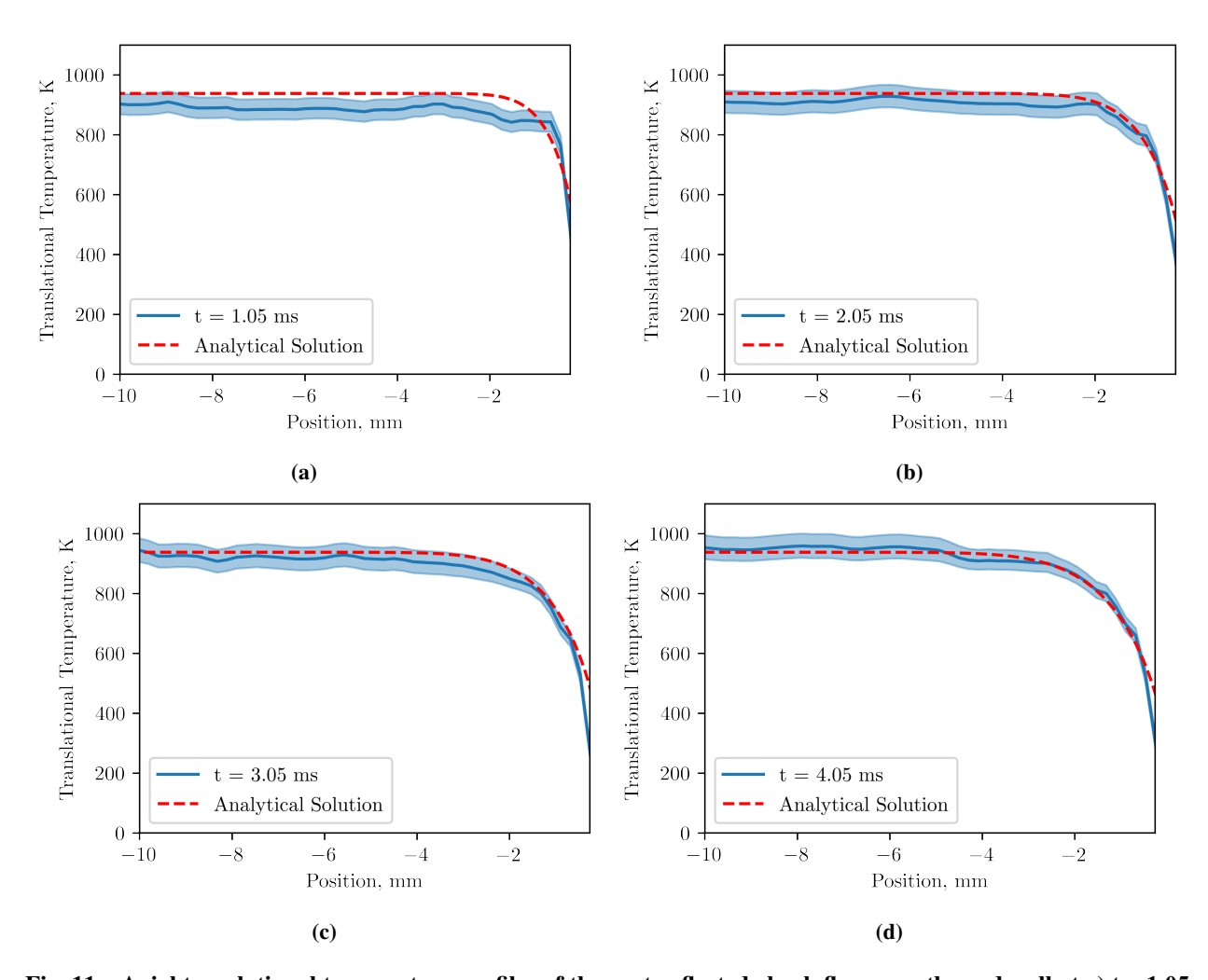


Fig. 11 Axial translational temperature profiles of the post-reflected-shock flow near the end wall at a) t = 1.05 ms, b) t = 2.05 ms, c) t = 3.05 ms, and d) t = 4.05 ms.

reasonable agreement with expected values. After the passage of the reflected shock, observations of the end-wall thermal boundary layer growth further showed good agreement with an established analytical solution.

While the unoptimized laser wavelength currently limits data quality, preliminary static and shock tube experiments nevertheless demonstrate that UV-LAI is a promising approach for obtaining full-field property information for highly dynamic one-dimensional flows and has strong potential for more complex future applications. As follow-up developments to the current prototype, additional wavelength selections will be performed to achieve higher temperature sensitivities at conditions of interest, and a second laser wavelength will be implemented for extending NO thermometry into reactive flows where X_{NO} is unknown or changing, or T_{vib} is unknown. Characterizations of the UV intensifier's transient response may enable corrections for possible non-linearity in image intensities to yield more quantitative results. More complex flow scenarios, such as reflected shock bifurcation and supersonic flow over bodies, will also be investigated in future studies.

Acknowledgments

This work was supported by the U.S. National Science Foundation under award number 1940865, contract monitor Dr. John Daily, and by the Air Force Office of Scientific Research through AFOSR grant FA9550-16-1-0291 with contract monitors Dr. I. Leyva and Dr. S. Popkin.

References

- [1] Mach, E., and Salcher, P., "Photographische Fixirung der durch Projectile in der Luft eingeleiteten Vorgänge," *Annalen der Physik*, Vol. 268, 1886, pp. 277–291. https://doi.org/10.1002/andp.18872681008.
- [2] Settles, G., Schlieren and Shadowgraph Techniques: Visualizing Phenomena in Transparent Media, Springer Science, 2001.
- [3] Hosch, J., and Walters, J., "High spatial resolution schlieren photography," *Applied optics*, Vol. 16, No. 2, 1977, pp. 473–482. https://doi.org/10.1364/AO.16.000473.
- [4] Kaiser, S., Salazar, V., and Hoops, A., "Schlieren Measurements in the Round Cylinder of an Optically Accessible Internal Combustion Engine," *Applied Optics*, Vol. 52, No. 14, 2013, p. 3433–3443. https://doi.org/10.1364/AO.52.003433.
- [5] Ben-Yakar, A., and Hanson, R., "Hypervelocity combustion studies using simultaneous OH-PLIF and schlieren imaging in an expansion tube," *35th joint propulsion conference and exhibit*, 1999, p. 2453. https://doi.org/10.2514/6.1999-2453.
- [6] Rossmann, T., Mungal, M., and Hanson, R., "Acetone PLIF and schlieren imaging of high compressibility mixing layers," *39th Aerospace Sciences Meeting and Exhibit*, 2001, p. 290. https://doi.org/10.2514/6.2001-290.
- [7] Casper, K. M., Beresh, S. J., Wagnild, R., Henfling, J., Spillers, R., and Pruett, B., "Simultaneous pressure measurements and high-speed schlieren imaging of disturbances in a transitional hypersonic boundary layer," 43rd AIAA Fluid Dynamics Conference, 2013, p. 2739. https://doi.org/10.2514/6.2013-2739.
- [8] Agrawal, A. K., Butuk, N. K., Gollahalli, S. R., and Griffin, D., "Three-dimensional rainbow schlieren tomography of a temperature field in gas flows," *Applied Optics*, Vol. 37, No. 3, 1998, pp. 479–485. https://doi.org/10.1364/AO.37.000479.
- [9] Satti, R. P., Kolhe, P. S., Olcmen, S., and Agrawal, A. K., "Miniature rainbow schlieren deflectometry system for quantitative measurements in microjets and flames," *Applied optics*, Vol. 46, No. 15, 2007, pp. 2954–2962. https://doi.org/10.1364/AO.46/002954
- [10] Kolhe, P., and Agrawal, A., "Density Measurements in a Supersonic Microjet Using Miniature Rainbow Schlieren Deflectometry," *AIAA Journal*, Vol. 47, 2009, p. 830–838. https://doi.org/10.2514/1.37332., no.
- [11] Hanson, R. K., "Planar laser-induced fluorescence imaging," *Journal of Quantitative Spectroscopy and Radiative Transfer*, Vol. 40, No. 3, 1988, pp. 343–362. https://doi.org/10.1016/0022-4073(88)90125-2.
- [12] McMillin, B., Lee, M., and Hanson, R., "Planar Laser-Induced Fluorescence Imaging of Shock-Tube Flows with Vibrational Nonequilibrium," *AIAA Journal*, Vol. 30, No. 2, 1992, p. 436–443. https://doi.org/10.2514/3.10935.
- [13] Skeen, S., Manin, J., and Pickett, L., "Simultaneous Formaldehyde PLIF and High-Speed Schlieren Imaging for Ignition Visualization in High-Pressure Spray Flames," *Proceedings of the Combustion Institute*, Vol. 35, No. 3, 2015, p. 3167–3174. https://doi.org/10.1016/j.proci.2014.06.040.
- [14] Hanson, R. K., Spearrin, R. M., and Goldenstein, C. S., Spectroscopy and optical diagnostics for gases, Vol. 1, Springer, 2016. https://doi.org/10.1007/978-3-319-23252-2_3.
- [15] Liu, X., Zhang, G., Huang, Y., Wang, Y., and Qi, F., "Two-Dimensional Temperature and Carbon Dioxide Concentration Profiles in Atmospheric Laminar Diffusion Flames Measured by Mid-Infrared Direct Absorption Spectroscopy at 4.2 m," Applied Physics B: Lasers and Optics, Vol. 124, 2018. https://doi.org/10.1007/s00340-018-6930-0.
- [16] Wei, C., Pineda, D., Paxton, L., Egolfopoulos, F., and Spearrin, R., "Mid-Infrared Laser Absorption Tomography for Quantitative 2D Thermochemistry Measurements in Premixed Jet Flames," *Applied Physics B: Lasers and Optics*, Vol. 124, No. 6, 2018. https://doi.org/10.1007/s00340-018-6984-z.
- [17] Foo, J., and Martin, P., "Tomographic Imaging of Reacting Flows in 3D by Laser Absorption Spectroscopy," *Applied Physics B: Lasers and Optics*, Vol. 123, No. 5, 2017. https://doi.org/10.1007/s00340-017-6733-8.
- [18] Zhang, Z., Sun, P., Pang, T., Xia, H., Cui, X., Li, Z., Han, L., Wu, B., Wang, Y., Sigrist, M., and Dong, F., "Reconstruction of Combustion Temperature and Gas Concentration Distributions Using Line-of-Sight Tunable Diode Laser Absorption Spectroscopy," *Optical Engineering*, Vol. 55, No. 7, 2016, p. 076107. https://doi.org/10.1117/1.oe.55.7.076107.
- [19] Ma, L., Cai, W., Caswell, A. W., Kraetschmer, T., Sanders, S. T., Roy, S., and Gord, J. R., "Tomographic imaging of temperature and chemical species based on hyperspectral absorption spectroscopy," *Optics express*, Vol. 17, No. 10, 2009, pp. 8602–8613. https://doi.org/10.1364/OE.17.008602.

- [20] Wang, F., Cen, K., Li, N., Jeffries, J., Huang, Q., Yan, J., and Chi, Y., "Two-Dimensional Tomography for Gas Concentration and Temperature Distributions Based on Tunable Diode Laser Absorption Spectroscopy," *Measurement Science and Technology*, Vol. 21, 2010. https://doi.org/10.1088/0957-0233/21/4/045301., no.
- [21] Wang, F., Wu, Q., Huang, Q., Zhang, H., Yan, J., and Cen, K., "Simultaneous Measurement of 2-Dimensional H2O Concentration and Temperature Distribution in Premixed Methane/Air Flame Using TDLAS-Based Tomography Technology," *Optics Communications*, Vol. 346, 2015, p. 53–63. https://doi.org/10.1016/j.optcom.2015.02.015.
- [22] Wei, C., Pineda, D., Goldenstein, C., and Spearrin, R., "Tomographic Laser Absorption Imaging of Combustion Species and Temperature in the Mid-Wave Infrared," *Optics Express*, Vol. 26, No. 16, 2018, p. 20944. https://doi.org/10.1364/oe.26.020944.
- [23] Schwarm, K., Wei, C., Pineda, D., and Mitchell Spearrin, R., "Time-Resolved Laser Absorption Imaging of Ethane at 2 KHz in Unsteady Partially Premixed Flames," *Applied Optics*, Vol. 58, No. 21, 2019, p. 5656. https://doi.org/10.1364/ao.58.005656.
- [24] Tancin, R., Spearrin, R., and Goldenstein, C., "2D Mid-Infrared Laser-Absorption Imaging for Tomographic Reconstruction of Temperature and Carbon Monoxide in Laminar Flames," *Optics Express*, Vol. 27, No. 10, 2019, p. 14184. https://doi.org/10.1364/oe.27.014184.
- [25] Qi, W., Zhou, Y., and Zhang, Y., "An Optical Diagnostic Technique Based on Ultraviolet Absorption and Schlieren for Components Stratification in a Binary-Component Fuel-Air Mixture," *Experiments in Fluids*, Vol. 61, No. 11, 2020. https://doi.org/10.1007/s00348-020-03063-w.
- [26] Qi, W., and Zhang, Y., "A Three-Color Absorption/Scattering Imaging Technique for Simultaneous Measurements on Distributions of Temperature and Fuel Concentration in a Spray," *Experiments in Fluids*, Vol. 59, 2018. https://doi.org/10.1007/s00348-018-2525-0.
- [27] Gao, J., and Nishida, K., "Laser Absorption-Scattering Technique Applied to Asymmetric Evaporating Fuel Sprays for Simultaneous Measurement of Vapor/Liquid Mass Distributions," *Applied Physics B: Lasers and Optics*, Vol. 101, No. 1–2, 2010, p. 433–443. https://doi.org/10.1007/s00340-010-4059-x.
- [28] Qi, W., and Zhang, Y., "Quantitative Measurement of Binary-Component Fuel Vapor Distributions via Laser Absorption and Scattering Imaging," *Applied Physics B: Lasers and Optics*, Vol. 125, 2019. https://doi.org/10.1007/s00340-019-7237-5.
- [29] Zhang, Y., and Nishida, K., "Vapor Distribution Measurement of Higher and Lower Volatile Components in an Evaporating Fuel Spray via Laser Absorption Scattering (LAS) Technique," *Combustion Science and Technology*, Vol. 179, No. 5, 2007, p. 863–881. https://doi.org/10.1080/00102200600672037.
- [30] Zhang, Y., and Nishida, K., "Vapor Distribution Measurement of Higher and Lower Volatile Components in an Evaporating Fuel Spray via Laser Absorption Scattering (LAS) Technique," Combustion Science and Technology, Vol. 179, No. 5, 2007, p. 863–881. https://doi.org/10.1080/00102200600672037.
- [31] Burke, R. F., Rezzag, T., and Ahmed, K. A., "Validation of Experimental Evidence for H2/O2 Powered Rotating Detonation Rocket Engine," *AIAA Propulsion and Energy 2021 Forum*, 2021, p. 3672.
- [32] Liu, X., Wang, Y., Wang, Z., and Qi, F., "Single camera high repetition rate two-color formaldehyde planar laser-induced fluorescence thermometry with a wavelength-switching burst mode laser," arXiv preprint arXiv:2108.03182, 2021.
- [33] Hsu, P. S., Slipchenko, M. N., Jiang, N., Fugger, C. A., Webb, A. M., Athmanathan, V., Meyer, T. R., and Roy, S., "Megahertz-rate OH planar laser-induced fluorescence imaging in a rotating detonation combustor," *Optics Letters*, Vol. 45, No. 20, 2020, pp. 5776–5779. https://doi.org/10.1364/OL.403199.
- [34] Falcone, P., Hanson, R., and Kruger, C., "Tunable Diode Laser Absorption Measurements of Nitric Oxide in Combustion Gases," *Combustion Science and Technology*, Vol. 35, No. 1–4, 1983, p. 81–99. https://doi.org/10.1080/00102208308923704.
- [35] Trad, H., Higelin, P., and Mounaim-Rousselle, C., "Nitric Oxide Detection inside the Cylinder of an SI Engine by Direct UV Absorption Spectroscopy," *Optics and Lasers in Engineering*, Vol. 43, No. 1, 2005, p. 1–18. https://doi.org/10.1016/j.optlaseng [2004.06.006.]
- [36] Anderson, T., Lucht, R., Priyadarsan, S., Annamalai, K., and Caton, J., "In Situ Measurements of Nitric Oxide in Coal-Combustion Exhaust Using a Sensor Based on a Widely Tunable External-Cavity GaN Diode Laser," *Applied Optics*, Vol. 46, No. 19, 2007, p. 3946–3957. https://doi.org/10.1364/AO.46.003946.
- [37] Bose, D., and Candler, G., "Advanced Model of Nitric Oxide Formation in Hypersonic Flows," *Journal of Thermophysics and Heat Transfer*, Vol. 12, No. 2, 1998, p. 214–222. https://doi.org/10.2514/2.6324.

- [38] Kliner, D., Koplow, J., and Goldberg, L., "Development of a Narrow-Band, Tunable, Frequency-Quadrupled Diode Laser for UV Absorption Spectroscopy," Applied Optics, Vol. 37, No. ue 18, 1998, pp. 3954–3960, https://doi.org/10.1364/AO.37.003954.
- [39] Campbell, M. F., Tulgestke, A. M., Davidson, D. F., and Hanson, R. K., "A second-generation constrained reaction volume shock tube," *Review of Scientific Instruments*, Vol. 85, No. 5, 2014, p. 055108. https://doi.org/10.1063/1.4875056.
- [40] Campbell, M. F., Owen, K. G., Davidson, D. F., and Hanson, R. K., "Dependence of calculated postshock thermodynamic variables on vibrational equilibrium and input uncertainty," *Journal of Thermophysics and Heat Transfer*, Vol. 31, No. 3, 2017, pp. 586–608. https://doi.org/10.2514/1.T4952
- [41] Wray, K. L., "Shock-Tube Study of the Vibrational Relaxation of Nitric Oxide," The Journal of Chemical Physics, Vol. 36, No. 10, 1962, pp. 2597–2603. https://doi.org/10.1063/1.1732339.
- [42] Krish, A., Streicher, J., and Hanson., R., "Spectrally-Resolved Ultraviolet Absorption Measurements of Shock-Heated NO from 2000 K to 6000 K for the Development of a Rotational Temperature Diagnostic," *Manuscript Submitted for Publication in Journal of Quantitative and Radiative Transfer*, 2022.
- [43] Greenberg, P. S., and Ku, J. C., "Soot volume fraction imaging," *Applied optics*, Vol. 36, No. 22, 1997, pp. 5514–5522. https://doi.org/10.1364/AO.36.005514.
- [44] Westlye, F., Penney, K., Ivarsson, A., Pickett, L., Manin, J., and Skeen, S., "Diffuse Back-Illumination Setup for High Temporally Resolved Extinction Imaging," *Applied Optics*, Vol. 56, No. 17, 2017, p. 5028. https://doi.org/10.1364/ao.56.005028.
- [45] Otsu, N., "A threshold selection method from gray-level histograms," *IEEE transactions on systems, man, and cybernetics*, Vol. 9, No. 1, 1979, pp. 62–66.
- [46] Bethe, H. A., and Teller, E., "Deviations from thermal equilibrium in shock waves," Tech. Rep. No. X-117, Ballistic Research Laboratory, 1941.
- [47] Williams, T. C., and Shaddix, C. R., "Simultaneous correction of flat field and nonlinearity response of intensified charge-coupled devices," *Review of Scientific Instruments*, Vol. 78, No. 12, 2007, p. 123702. https://doi.org/10.1063/1.2821616.
- [48] Böhm, B., Heeger, C., Gordon, R. L., and Dreizler, A., "New perspectives on turbulent combustion: multi-parameter high-speed planar laser diagnostics," *Flow, turbulence and combustion*, Vol. 86, No. 3-4, 2011, pp. 313–341. https://doi.org/10.1007/s10494-010-9291-2.
- [49] Van Dongen, M. E. H., "Thermal diffusion effects in shock tube boundary layers," Ph. D. Thesis, 1978.